


 Cite this: *RSC Adv.*, 2022, 12, 10863

# All-vacuum deposited perovskite solar cells with glycine modified NiO<sub>x</sub> hole-transport layers†

 Cheng Fang,<sup>a</sup> Qianqian Zhao,<sup>a</sup> Fuping Zhao,<sup>a</sup> Fuzhi Huang,<sup>ab</sup> Yong Peng,<sup>a</sup> Zhiliang Ku,<sup>ab\*</sup> Yi-Bing Cheng<sup>b</sup> and Zhengyi Fu<sup>ab\*</sup>

Organic–inorganic hybrid perovskite solar cells (PSCs) have attracted enormous research attention due to their high efficiency and low cost. However, most of the PSCs with high efficiencies still need expensive organic materials as their hole-transport layer (HTL). Obviously, the highly expensive materials go against the low-cost concept of advanced PSCs. In this regard, inorganic NiO<sub>x</sub> was considered as an idea HTL due to its good transmittance in the visible region and outstanding chemical stability. But for most of the PSCs with a NiO<sub>x</sub> HTL, the hole-extraction efficiency was limited by the unmatched valence band and too many surface defects of the NiO<sub>x</sub> layer, especially for the vacuum-deposited NiO<sub>x</sub> and perovskite. Herein, we developed a facile strategy to overcome this issue by using self-assembled glycine molecules to treat the NiO<sub>x</sub> surface. With glycine on the surface, the NiO<sub>x</sub> exhibited a deeper valence band maximum and a faster charge-extraction at the NiO<sub>x</sub>/perovskite interface. What's more, the vacuum-deposited perovskite showed a better crystallinity on the NiO<sub>x</sub> + glycine substrate. As a result, the PSCs with a glycine interfacial layer achieved a champion PCE of 17.96% with negligible hysteresis. This facile approach is expected to be further developed for fabricating high-efficiency PSCs on textured silicon solar cells.

 Received 1st March 2022  
 Accepted 30th March 2022

DOI: 10.1039/d2ra01360f

[rsc.li/rsc-advances](http://rsc.li/rsc-advances)

## Introduction

In the past decade, perovskite solar cells (PSCs) have experienced a rapid development with their power conversion efficiency (PCE) soaring from 3.8% to 25.7%.<sup>1,2</sup> The high PCE together with the low-cost raw materials make PSCs the most promising photovoltaic (PV) technique among the third-generation PV technologies. Currently, most of the PSCs with high PCEs generally employ highly expensive organic materials such as 2,2',7,7'-tetrakis[*N,N*-di(4-methoxyphenyl)amino]-9,9'-spirobifluorene (Spiro-OMeTAD)<sup>3</sup> and poly[bis(4-phenyl)(2,4,6-trimethylphenyl)amine] (PTAA)<sup>4</sup> as their hole transport layer (HTL). Clearly, the use of highly expensive materials goes against the low-cost concept for advanced PV techniques. What's more, these organic materials suffer from instability issues when operated for longer times at elevated temperatures.<sup>5</sup> In particular, the Spiro-OMeTAD is known to cause major device degradation if exposed to moisture<sup>6</sup> or temperatures above 60 °C,<sup>7</sup> which is a typical operating temperature of solar modules. Additionally, the hydrophilic dopant-ions in

Spiro-OMeTAD and metal atoms of the electrode can easily penetrate through the Spiro-OMeTAD layer and diffuse into the perovskite layer, causing PCE decay of the device. Hence, developing a low-cost and stable inorganic HTL layer is critical for the industrial application of PSCs. So far, several inorganic oxides including copper oxide (CuO<sub>x</sub>),<sup>8</sup> nickel oxide (NiO<sub>x</sub>),<sup>9</sup> vanadium pentoxide (V<sub>2</sub>O<sub>5</sub>)<sup>10</sup> and molybdenum oxide (MoO<sub>x</sub>)<sup>11</sup> have been used as HTL in PSCs. Among these metal oxides, NiO<sub>x</sub> has drawn most attention due to its good transmittance in visible region and outstanding chemical stability. Generally, NiO<sub>x</sub> thin-films can be prepared by solution-based chemical process and vacuum-based physical deposition. As early in 2014, Zhu and co-authors reported a sol-gel method to synthesis NiO<sub>x</sub> nanocrystals and used them as HTLs in PSCs.<sup>12</sup> After that, several other chemical deposition methods including solution combustion,<sup>13</sup> electrochemical deposition,<sup>14</sup> chemical bath deposition,<sup>15</sup> atomic layered deposition<sup>16</sup> and spray-pyrolysis deposition<sup>17</sup> have been developed to prepared NiO<sub>x</sub> thin films for PSCs. Chen and co-authors employed contrivable molecules to tailor the conductivity and energy level of NiO<sub>x</sub> nanoparticles and achieved 22.1% of PCE in PSCs, which is a record PCE for NiO<sub>x</sub>-based PSCs to date.<sup>18</sup> Apart from the chemical deposition processes, physical vacuum deposition techniques such as pulsed laser deposition,<sup>19</sup> electron beam evaporation<sup>20</sup> and sputtering<sup>21</sup> are also employed to deposit NiO<sub>x</sub> thin films with highly controllable thickness and nano-structured morphology. Note that, these vacuum-based

<sup>a</sup>State Key Laboratory of Advanced Technologies for Materials Synthesis and Processing, Wuhan University of Technology, 122 Luoshi Road, Wuhan 430070, Hubei Province, China. E-mail: zhiliang.ku@whut.edu.cn; zyfu@whut.edu.cn

<sup>b</sup>Foshan Xianhu Laboratory of the Advanced Energy Science and Technology Guangdong Laboratory, Foshan 528216, Guangdong Province, China

† Electronic supplementary information (ESI) available. See DOI: 10.1039/d2ra01360f



deposition techniques, which have been widely used in thin-film industry, are mature enough for promoting the commercial development of PSCs. Especially for the silicon/perovskite tandem devices, vacuum-based deposition techniques possess unique advantages in depositing conformal thin film on the textured silicon solar cell surface. However, most of the PSCs with vacuum deposited  $\text{NiO}_x$  still need solution-processed perovskite to achieve high PCE. Tobias and co-authors compared the PSCs with perovskite layer deposited by co-evaporation, spin coating and inkjet printing.<sup>22</sup> They found that the device with inkjet-printed perovskite exhibited high PCE up to 19.5%, whereas the device with spin-coated perovskite showed significant lower PCE of 17.3%. And with co-evaporated perovskite, the device PCE further reduced to 15.1%. This is mainly due to the poor charge-extraction efficiency at the perovskite and  $\text{NiO}_x$  interface. Caleb C. and co-authors revealed that  $\text{Ni}^{\geq 3+}$  metal cation sites in the  $\text{NiO}_x$  thin films act both as Brønsted proton acceptors and Lewis electron acceptors, deprotonating cationic amines and oxidizing iodide species, forming  $\text{PbI}_2$ -rich hole extraction barriers at the perovskite- $\text{NiO}_x$  interface.<sup>23</sup> They also developed a facile approach to eliminate the barriers, which achieved by reacting  $\text{Ni}^{\geq 3+}$  with excess formamidinium iodide (FAI) during perovskite active layer deposition. Obviously, this electrochemical reduction of  $\text{Ni}^{\geq 3+}$  defects can be facilitated by the perovskite solution which is rich in  $\text{FA}^+$  and  $\text{I}^-$  ions. But for the perovskites deposited by vacuum-based techniques, the  $\text{Ni}^{\geq 3+}$  surface states can't be eliminated effectively, causing low device performance.<sup>22</sup> Thus, seeking new surface treatment to enhance the charge-extraction efficiency between the vacuum-deposited  $\text{NiO}_x$  and perovskite thin films is of great significance for large-area and low-cost PSCs with high efficiency. Recently, Zhang *et al.* introduced tris(2-methyl-1-aziridinepropionate) as a barrier layer at the interface between perovskite and  $\text{NiO}_x$ , successfully inhibited the reaction of  $\text{Ni}^{\geq 3+}$  with MAI and improved the device voltage to 1.12 V.<sup>24</sup>  $\text{NiOOH}$  is a typical  $\text{Ni}^{\geq 3+}$  compound that exists on the surface of  $\text{NiO}_x$  and is prepared by the combination of the surface hydroxyl group with Ni. Zhao *et al.*, coated  $\text{NiO}_x$  surface with pyridine carboxylic acid to anchor hydroxyl on the surface, thereby eliminating hydroxyl.<sup>25</sup> In addition, Zheng *et al.* demonstrated that such surface treatment is also feasible in tandem devices.<sup>26</sup> To overcome the poor scaling-up ability of spin-coating, Phung *et al.* immersed the  $\text{NiO}_x$  substrates into MeO-2PACz solution, and assembled MeO-2PACz monolayer on the surface of  $\text{NiO}_x$ .<sup>27</sup> Clearly, in comparison with spin-coating, such soaking process in solution is more in favor of assembling monolayer on large-area substrate.

Inspired by the above works, herein, we employed vacuum and vapor-based techniques to prepare all the functional layers of PSCs, aiming at fabricating silicon/perovskite tandem solar cell with textured silicon substrate. The  $\text{NiO}_x$  thin films were deposited by electron beam evaporation and used as the HTL layers.  $\text{PbI}_2/\text{CsBr}$  inorganic frameworks were deposited by thermal evaporation and then be treated in FAI vapor to obtain  $\text{Cs}_{0.14}\text{FA}_{0.86}\text{Pb}(\text{Br}_x\text{I}_{1-x})_3$  perovskite. Both the electron transport layer (ETL) and Ag electrode were deposited by thermal evaporation. As mentioned above, this all-vacuum deposited PSCs

suffer from low PCE due to the poor hole-extraction ability of  $\text{NiO}_x$  film. To address this issue, we herein employed glycine ( $\text{NH}_2\text{CH}_2\text{COOH}$ ), self-assembly molecule, as an interfacial modifier between the as-prepared  $\text{NiO}_x$  and perovskite film to passivate the surface defect and enhance the hole-extraction. Glycine is amphoteric molecule which has one amino group and one carboxyl group. The carboxyl group can be anchored with the exposed hydroxy group on the  $\text{NiO}_x$  surface,<sup>28</sup> and carboxyl group is a typical electron withdrawing group<sup>29</sup> can increasing the work function of  $\text{NiO}_x$ . It's noteworthy that although various organic molecules<sup>30-33</sup> have been used to modify  $\text{NiO}_x$  HTL in PSCs, there have been very few attempts to use amphoteric molecules in all-vacuum deposited PSCs. By optimizing the chemisorption time, we fabricated planar PSCs with  $\text{NiO}_x/\text{glycine}/\text{perovskite}/\text{ETL}/\text{Ag}$  inverted structure. The champion device exhibited a champion PCE of 17.96% with the open circuit voltage ( $V_{oc}$ ) improved from 0.995 V to 1.040 V and fill factor (FF) improved from 0.72 to 0.77, indicating a significant faster hole-extraction at the  $\text{NiO}_x/\text{glycine}/\text{perovskite}$  interface.

## Results and discussion

The  $\text{NiO}_x$  films with thickness of 35 nm were deposited by electron beam evaporation on fluorine doped tin oxide (FTO) glasses. Glycine monolayer was self-assembled on  $\text{NiO}_x$  surface by immersing the  $\text{NiO}_x$  films into glycine/ $\text{H}_2\text{O}$  solution. To ensure the fully chemisorption of glycine on  $\text{NiO}_x$ , we performed the immersion with different time length and measured the contact angles of the samples. As presented in Table S1,† after 90 min of immersion, the contact angle of the samples increased from 23.75° to 69.61° (Fig. 1a), and maintained at around 69° with another 60 min of immersion, indicating the chemisorption of glycine was saturated at 90 min. Thus, 90 min was selected as the suitable duration for glycine self-assembling. The optical transmittance spectra of the  $\text{NiO}_x$  film with and without glycine were measured by UV-vis spectroscopy (Fig. 1b). With glycine on the surface, the FTO/ $\text{NiO}_x$  + glycine sample showed a slightly higher transmittance than that of the FTO/ $\text{NiO}_x$  control sample over a broad spectral range (400 nm to 800 nm). To further investigate the interaction of glycine with the  $\text{NiO}_x$ , X-ray photoelectron spectroscopy (XPS) was performed on the  $\text{NiO}_x$  with and without glycine. The spectra of the N 1s peak of samples are shown in Fig. S1.† Compared with pristine  $\text{NiO}_x$ , the N 1s peak around 400 eV in the  $\text{NiO}_x$  + glycine sample can be clearly observed, which belonging to the  $-\text{NH}_2$  group.<sup>31</sup> Fig. 1c and d shows XPS spectra of Ni 2p<sub>3/2</sub> core level for the pristine  $\text{NiO}_x$  film and the  $\text{NiO}_x$  + glycine film. For the pristine  $\text{NiO}_x$ , the two peaks at binding energy of 854.09 eV and 855.74 eV correspond to  $\text{Ni}^{2+}$  and  $\text{Ni}^{3+}$ .<sup>34</sup> After glycine treatment, both the two peaks have reduced and located at lower binding energy of 853.76 eV and 855.42 eV, respectively, which indicates that the electronic environment near the Ni atom has changed. In the O 1s XPS spectra of Fig. S2,† In the pristine  $\text{NiO}_x$ , the ratio of adsorbed oxygen (originating from the chemisorbed oxygen atoms or hydroxyl groups on the  $\text{NiO}_x$  film) to lattice oxygen was 0.82. After being



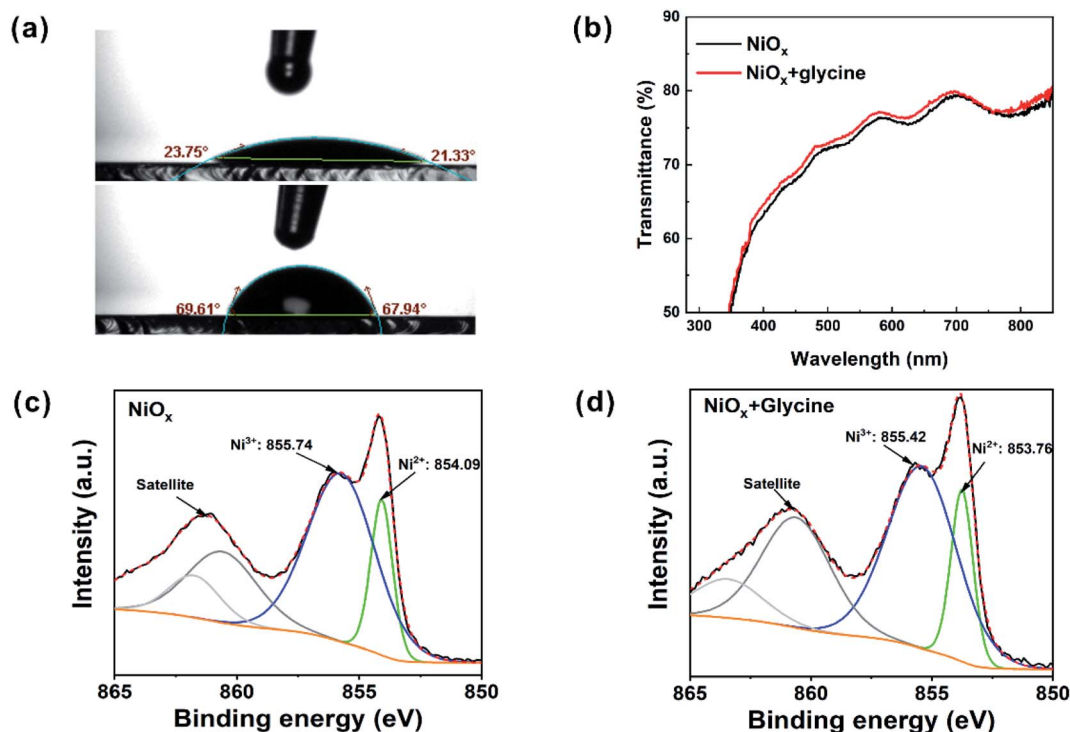


Fig. 1 Contact angle measurements in (a), transmission spectra in (b) and XPS spectra in (c) and (d) of the NiO<sub>x</sub> and NiO<sub>x</sub> + glycine films.

treated with glycine, this ratio increased to 0.91, indicating the adsorbed oxygen on the NiO<sub>x</sub> surface increased.

These results suggest that the interaction between glycine and NiO<sub>x</sub> is realized by the anchoring between -COOH and -OH groups rather than by the hydrogen bond of -NH<sub>2</sub> on NiO<sub>x</sub> (-NH<sup>3+</sup>).<sup>35</sup> Thus, we can deduce that the carboxyl group of glycine reacts with the hydroxyl group on the surface of NiO<sub>x</sub> to form a self-assembled monolayer (Fig. 2a). Ultraviolet photoelectron spectrometer (UPS) measurement was employed to investigate the work function and valence band changes of the NiO<sub>x</sub> + glycine film. The UPS results for the secondary electron cutoff ( $E_{\text{cutoff}}$ ) region and HOMO region ( $E_{\text{HOMO}}$ ) are shown in Fig. 2b. The valence band ( $E_{\text{VB}}$ ) can be obtained by using the equation  $E_{\text{VB}} = h\nu - (E_{\text{cutoff}} - E_{\text{HOMO}})$  ( $h\nu = 21.22$  eV),  $\text{WF} = h\nu - E_{\text{cutoff}}$ .<sup>36</sup> The work function is calculated to be 4.52 eV for pristine NiO<sub>x</sub> film while that of the NiO<sub>x</sub> + glycine film increased to it 4.72 eV. Accordingly, the  $E_{\text{VB}}$  of NiO<sub>x</sub> + glycine was -5.43 eV,

which has a downward shift by 0.22 eV in comparison with the pristine NiO<sub>x</sub> (-5.21 eV). As a result, there is a favorable energy level alignment for extraction of holes from perovskite to NiO<sub>x</sub> due to lower  $E_{\text{VB}}$  of glycine-modified NiO<sub>x</sub> (Fig. 2c).

CS<sub>0.14</sub>FA<sub>0.86</sub>Pb(Br<sub>x</sub>I<sub>1-3</sub>)<sub>3</sub> perovskite films were prepared by vapor-solid reaction method,<sup>37</sup> which combines a thermal evaporation process and a vapor sublimation process. X-ray diffraction (XRD) characterization was employed to identify the crystal structure of the as-prepared perovskite films. As shown in Fig. S3,† the perovskite film on NiO<sub>x</sub> substrate exhibited a series diffraction peaks at  $2\theta = 14.0^\circ$ ,  $28.2^\circ$  and  $31.6^\circ$ , which should attribute to the (001), (002) and (012) crystal planes of the cubic  $\alpha$ -FAPbI<sub>3</sub>,<sup>38</sup> respectively. And a small peak at  $2\theta = 12.7^\circ$  can also be observed, indicating the residual PbI<sub>2</sub> in the perovskite. For the perovskite film on NiO<sub>x</sub> + glycine substrate, the diffraction peaks of perovskite showed stronger intensities, indicating a better crystallinity of perovskite.

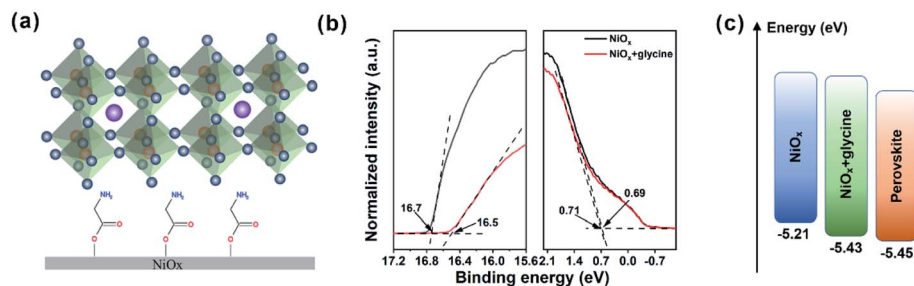


Fig. 2 Diagram of glycine interlayer between NiO<sub>x</sub> HTL and perovskite (a), UPS spectra of NiO<sub>x</sub> and NiO<sub>x</sub> + glycine films (b) and energy band diagram of corresponding materials used in the solar device (c).



Moreover, no obvious residual  $\text{PbI}_2$  can be observed in the pattern. We deduced that the exposed  $-\text{NH}_2$  group of glycine can affect the crystallization of perovskite and promote the transformation of  $\text{PbI}_2$  into perovskite. Scanning electron microscopy (SEM) measurements were performed on the samples to investigate the microstructure of perovskite films. From Fig. 3a and b, we can observe that the perovskite film on  $\text{NiO}_x$  substrate exhibited a compact morphology and grain sizes varying from 200–700 nm. With glycine on the substrate, the perovskite became more uniform with larger grain sizes, manifesting an improved crystallinity. To confirm this, we fabricated hole-only devices with structure of FTO/ $\text{NiO}_x$ (+glycine)/perovskite/PTAA/Ag and employed space charge limited current (SCLC) method to evaluate the trap densities in the two perovskite films. As shown in Fig. 3c and d, the defect density ( $N_t$ ) was calculated from the SCLC plot by using the Mott–Gurney equation:<sup>39</sup>  $V_{\text{TFL}} = eN_t L^2 / 2\epsilon\epsilon_0$ , where  $e$  is the elementary charge,  $N_t$  is the defect density,  $L$  is the thickness of the perovskite film,  $\epsilon$  is the relative dielectric constant of perovskite material, the  $\epsilon_0$  is the vacuum permittivity. The  $V_{\text{TFL}}$  of the devices without and with glycine treatment are fitted as 1.12 V and 0.61 V, respectively. Accordingly, the defect density decreased from  $1.58 \times 10^{-16} \text{ cm}^{-3}$  ( $\text{NiO}_x$ ) to  $8.63 \times 10^{-15} \text{ cm}^{-3}$  ( $\text{NiO}_x$  + glycine).

Steady-state photoluminescence (PL) and time-resolved photoluminescence (TRPL) measurements were performed on the FTO/ $\text{NiO}_x$ /perovskite and FTO/ $\text{NiO}_x$  + glycine/perovskite samples to further understand the non-radiative recombination process. From Fig. 4a, we can clearly see that, with  $\text{NiO}_x$  + glycine quenching layer, the PL intensity is significantly lower

than that of the sample with pristine  $\text{NiO}_x$ , which represents more efficient charge extraction and a superior transportation capacity at the glycine-treated  $\text{NiO}_x$  and perovskite interface. The TRPL results (Fig. 4b) were fitted by using a bi-exponential decay function:  $Y = A_1 \exp(-t/\tau_1) + A_2 \exp(-t/\tau_2) + y_0$ , where  $A_1$  and  $A_2$  are relative amplitudes and  $\tau_1$  and  $\tau_2$  are the lifetimes for fast and slow recombination, respectively. The  $\tau_1$  is typically associated with surface recombination, and the  $\tau_2$  is mainly due to recombination in the body of perovskite.<sup>40</sup> As summarized in Table S2,<sup>†</sup> the  $\text{NiO}_x$  + glycine/perovskite film possessed a smaller  $\tau_1$  (37 ns) than that of the sample without glycine (58 ns), indicating faster charge extraction at the interface of the  $\text{NiO}_x$  + glycine/perovskite. Meanwhile, the longer  $\tau_2$  of  $\text{NiO}_x$  + glycine/perovskite film confirms the lower trap density in the perovskite deposited on  $\text{NiO}_x$  + glycine substrate. We fabricated PSCs with an inverted architecture of FTO/ $\text{NiO}_x$ /perovskite/C60/BCP/Ag. Fig. 4c presents the current density–voltage ( $J$ – $V$ ) curves of the PSCs measured under AM 1.5G illumination. The device without glycine treatment yielded a champion PCE of 15.27% from reverse scan with an open-circuit voltage ( $V_{\text{oc}}$ ) of 995 mV, a short-circuit current density ( $J_{\text{sc}}$ ) of  $21.31 \text{ mA cm}^{-2}$  and a fill factor (FF) of 0.72. With glycine interfacial layer, the device exhibited an improved  $V_{\text{oc}}$  of 1040 mV and FF of 0.77, rendering a champion PCE of 17.96% with negligible hysteresis. Although such PCE is a big progress for the all-vacuum processed inverted PSCs, in comparison with other state-of-the-art inverted PSCs (see Table S3<sup>†</sup>) with  $\text{NiO}_x$  HTL, our devices need further improvements. Incident-photon-to-current efficiency (IPCE) spectra was employed to identify the current density of the champion devices. As shown in Fig. 4d, the glycine-modified

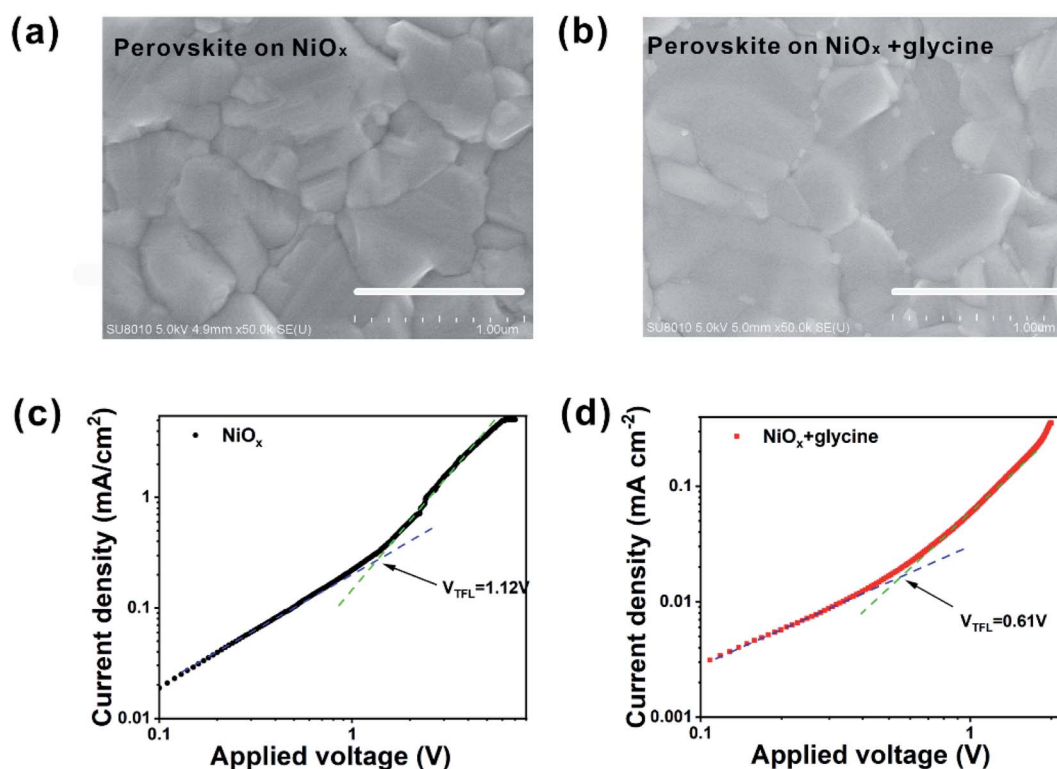


Fig. 3 SEM images in (a) and (b), dark  $J$ – $V$  curves of the hole-only devices in (c) and (d) based on the  $\text{NiO}_x$  and  $\text{NiO}_x$  + glycine films.



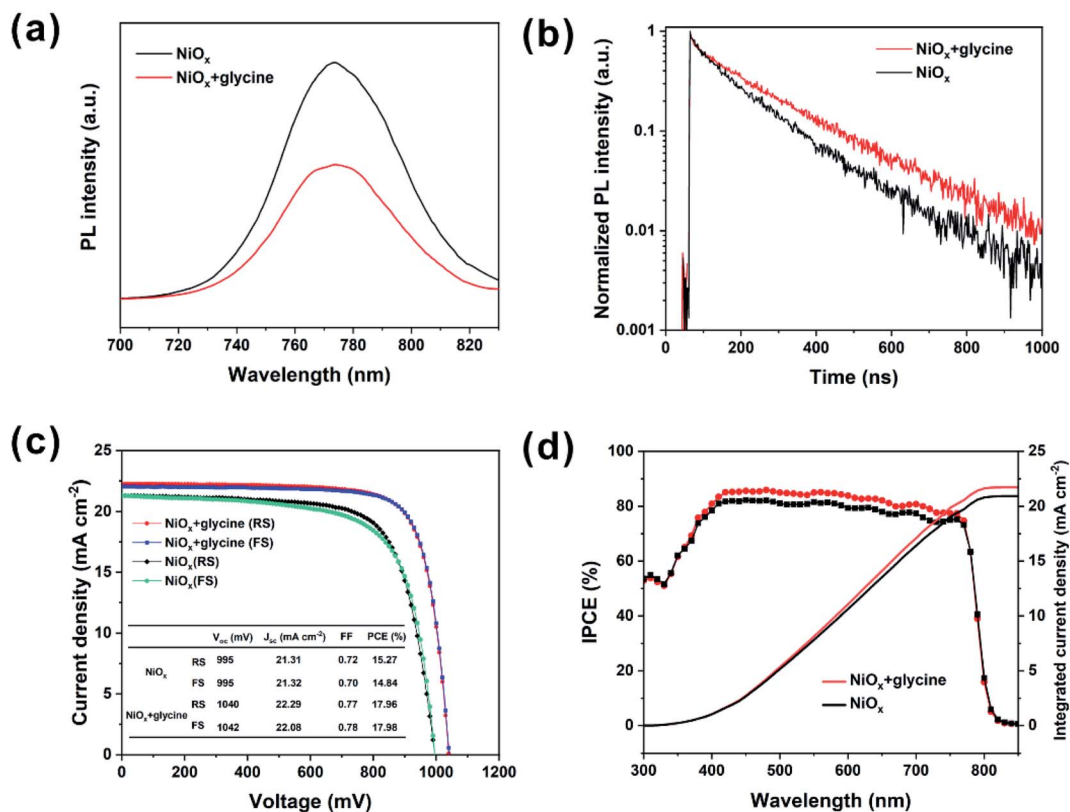


Fig. 4 The PL spectra (a), TRPL spectra (b),  $J$ - $V$  curves (c) and IPCE spectra (d) of the devices based on the NiO<sub>x</sub> and NiO<sub>x</sub> + glycine films.

device exhibited a higher IPCE value at the wavelength range of 420–770 nm. As a result, the integrated current density of the glycine-modified device reached 21.97 mA cm<sup>-2</sup> and the control device was 20.94 mA cm<sup>-2</sup>, which was quite in agreement with the  $J_{sc}$  derived from the  $J$ - $V$  curve.

## Conclusions

In summary, we fabricated perovskite solar cells by using all-vacuum processing methods, aiming at their further applications in perovskite/silicon tandem solar cells. Glycine was employed as a self-assemble monolayer to modify the electron-beam evaporated NiO<sub>x</sub> HTL layer. We found that the -COOH group in glycine can anchor with the -OH groups on NiO<sub>x</sub> surface, and lower the energy level of NiO<sub>x</sub> film. Moreover, the exposed -NH<sub>2</sub> groups of glycine molecules can also improve the crystallinity of the vacuum/vapor-deposited perovskite films. As a result, the devices with glycine interfacial layer achieved a champion PCE of 17.96%, which is significantly higher than that of the device without glycine. We believe such a facile surface treatment can provide ideas for fabricating high-efficiency PSCs based on NiO<sub>x</sub> HTL and merits future work.

## Experimental

### Materials

All the reagents and chemicals were used as received, including formamidinium halide (FAI, purity > 99%, Suzhou Xurou

Optoelectronics Technology Corp.), lead iodide (PbI<sub>2</sub>, purity > 99.99%), cesium iodide (CsI, purity > 99.9%) and glycine were purchased from Xi'an Polymer Light Technology Corp. All the other materials were purchased from Sigma or Aldrich without any purification.

### Preparation of NiO<sub>x</sub> and NiO<sub>x</sub> + glycine substrates

FTO glasses were first etched by employing a femtosecond laser (Universal Laser Systems, VLS2.30), and the glasses were ultrasonically cleaned with detergent, deionized water, and anhydrous ethanol, respectively. And then the substrates were under plasma clean treatment for 15 min before evaporation. The NiO<sub>x</sub> films were prepared by electron-beam evaporation at  $9 \times 10^{-4}$  Pa. The growth rate was controlled at  $0.1 \text{ \AA s}^{-1}$ , and the thickness was 35 nm. For glycine surface passivation, the as-prepared NiO<sub>x</sub> films were dipped for different times in the glycine/H<sub>2</sub>O solution with a concentration of  $0.75 \text{ mg ml}^{-1}$  and then rinsed by deionized water. After being dried with compressed air, the substrates were heated on the hotplate at 100 °C for 15 min in N<sub>2</sub>.

### Preparation of perovskite, ETL and electrode

CsBr (about  $0.3\text{--}0.5 \text{ \AA s}^{-1}$ , 30 nm) and PbI<sub>2</sub> (about  $3\text{--}5 \text{ \AA s}^{-1}$ , 300 nm) were deposited by thermal evaporation on the NiO<sub>x</sub> (+glycine) substrates in sequence. Then, the films were transferred into a CVD furnace and reacted with FAI/FAICl vapor, which generated by heating the pre-deposited (ultrasonic



spraying) FAI/FACl film on glass substrate. The temperature and pressure of the vapor–solid reaction were controlled at 160 °C and 50 Pa, respectively. After 30 min of reaction, we obtained the  $\text{Cs}_{0.14}\text{FA}_{0.86}\text{Pb}(\text{Br}_{x-1-x})_3$  perovskite. Then, C60 (25 nm) and BCP (8 nm) were thermally evaporated onto the perovskite film under high vacuum ( $<10^{-4}$  Pa). Finally, a 100 nm-thick layer of Ag was evaporated on the top of BCP as electrode.

### Characterization

X-ray photoelectron spectroscopy (XPS) were obtained using an X-ray photoelectron spectrometer (Thermo Scientific ESCALAB Xi<sup>+</sup>). The X-ray diffraction (XRD) patterns of the samples were recorded using an X-ray diffractometer (XRD, D8 Advance). The UV-vis measurements were carried out using UV-vis (lambda 750S, PerkinElmer). The steady-state photoluminescence (PL) and time-resolved photoluminescence (TRPL) spectra were obtained on an FLS1000 Photoluminescence Spectrometer (Edinburgh Instruments Ltd) equipped with double monochromators, a 450 W Xenon lamp, EPL-465 pulsed diode laser. The morphology was observed using field-emission scanning electron microscopy (FE-SEM, Hitachi SU8010). The dark  $I$ - $V$  curves of the hole-only devices using a solar simulator. The photocurrent density–voltage ( $J$ - $V$ ) curves of the perovskite solar cells were measured using a solar simulator (Oriel 94023A, 300 W) and a Keithley 2400 source meter. The intensity ( $100 \text{ mW cm}^{-2}$ ) was calibrated using a standard Si solar cell (Oriel, VLSI standards). All the devices were tested under AM 1.5G sun light ( $100 \text{ mW cm}^{-2}$ ), and the active area of  $0.147 \text{ cm}^2$  was defined by a metal mask. An external quantum efficiency (EQE) measurement system (QEX10, PV Measurements, Inc.) was used to measure the IPCE of the device across a wavelength range of 350–850 nm.

### Conflicts of interest

There are no conflicts to declare.

### Acknowledgements

The authors acknowledge the financial support by National Natural Science Foundation of China (NSFC 91963209, 51972251), The National Key Research and Development Plan (2019YFE0107200), Foshan Xianhu Laboratory of the Advanced Energy Science and Technology Guangdong Laboratory (XHD2020-001 and XHT2020-005) and the Fundamental Research Funds for the Central Universities (WUT: 2020III0242D).

### References

- 1 K. T. A. Kojima, Y. Shirai and T. Miyasaka, *J. Am. Chem. Soc.*, 2009, **131**, 6050–6051.
- 2 N. R. E. L. N., Best Research Cell\_Efficiencies, 2021, <https://www.nrel.gov/pv/cell-efficiency.html>.
- 3 H. Min, D. Y. Lee, J. Kim, G. Kim, K. S. Lee, J. Kim, M. J. Paik, Y. K. Kim, K. S. Kim, M. G. Kim, T. J. Shin and S. Il Seok, *Nature*, 2021, **598**, 444–450.
- 4 S. Chen, X. Dai, S. Xu, H. Jiao, L. Zhao and J. Huang, *Science*, 2021, **373**, 902–907.
- 5 K. Domanski, E. A. Alharbi, A. Hagfeldt, M. Grätzel and W. Tress, *Nat. Energy*, 2018, **3**, 61–67.
- 6 S. Ma, S. Pang, H. Dong, X. Xie, G. Liu, P. Dong, D. Liu, W. Zhu, H. Xi, D. Chen, C. Zhang and Y. Hao, *Polymers*, 2022, **14**, 343.
- 7 A. K. Jena, Y. Numata, M. Ikegami and T. Miyasaka, *J. Mater. Chem. A*, 2018, **6**, 2219–2230.
- 8 C. Zuo and L. Ding, *Small*, 2015, **11**, 5528–5532.
- 9 S. Bai, P. Da, C. Li, Z. Wang, Z. Yuan, F. Fu, M. Kawecki, X. Liu, N. Sakai, J. T.-W. Wang, S. Huettner, S. Buecheler, M. Fahlman, F. Gao and H. J. Snaith, *Nature*, 2019, **571**, 245–250.
- 10 D. Wang, N. K. Elumalai, M. A. Mahmud, M. Wright, M. B. Upama, K. H. Chan, C. Xu, F. Haque, G. Conibeer and A. Uddin, *Org. Electron.*, 2018, **53**, 66–73.
- 11 Z.-L. Tseng, L.-C. Chen, C.-H. Chiang, S.-H. Chang, C.-C. Chen and C.-G. Wu, *Sol. Energy*, 2016, **139**, 484–488.
- 12 Z. Zhu, Y. Bai, T. Zhang, Z. Liu, X. Long, Z. Wei, Z. Wang, L. Zhang, J. Wang, F. Yan and S. Yang, *Angew. Chem., Int. Ed.*, 2014, **53**, 12571–12575.
- 13 J. W. Jung, C.-C. Chueh and A. K.-Y. Jen, *Adv. Mater.*, 2015, **27**, 7874–7880.
- 14 I. J. Park, G. Kang, M. A. Park, J. S. Kim, S. W. Seo, D. H. Kim, K. Zhu, T. Park and J. Y. Kim, *ChemSusChem*, 2017, **10**, 2660–2667.
- 15 J. Sun, J. Lu, B. Li, L. Jiang, A. S. R. Chesman, A. D. Scully, T. R. Gengenbach, Y.-B. Cheng and J. J. Jasieniak, *Nano Energy*, 2018, **49**, 163–171.
- 16 S. Seo, I. J. Park, M. Kim, S. Lee, C. Bae, H. S. Jung, N.-G. Park, J. Y. Kim and H. Shin, *Nanoscale*, 2016, **8**, 11403–11412.
- 17 W. Chen, Y. Wu, Y. Yue, J. Liu, W. Zhang, X. Yang, H. Chen, E. Bi, I. Ashraful, M. Grätzel and L. Han, *Science*, 2015, **350**, 944–948.
- 18 P. Ru, E. Bi, Y. Zhang, Y. Wang, W. Kong, Y. Sha, W. Tang, P. Zhang, Y. Wu, W. Chen, X. Yang, H. Chen and L. Han, *Adv. Energy Mater.*, 2020, **10**, 1903487.
- 19 J. H. Park, J. Seo, S. Park, S. S. Shin, Y. C. Kim, N. J. Jeon, H.-W. Shin, T. K. Ahn, J. H. Noh, S. C. Yoon, C. S. Hwang and S. I. Seok, *Adv. Mater.*, 2015, **27**, 4013–4019.
- 20 W.-C. Lai, K.-W. Lin, Y.-T. Wang, T.-Y. Chiang, P. Chen and T.-F. Guo, *Adv. Mater.*, 2016, **28**, 3290–3297.
- 21 K.-C. Wang, P.-S. Shen, M.-H. Li, S. Chen, M.-W. Lin, P. Chen and T.-F. Guo, *ACS Appl. Mater. Interfaces*, 2014, **6**, 11851–11858.
- 22 T. Abzieher, S. Moghadamzadeh, F. Schackmar, H. Eggers, F. Sutterlütli, A. Farooq, D. Kojda, K. Habicht, R. Schmager, A. Mertens, R. Azmi, L. Klotz, J. A. Schwenzler, M. Hetterich, U. Lemmer, B. S. Richards, M. Powalla and U. W. Paetzold, *Adv. Energy Mater.*, 2019, **9**, 1802995.
- 23 C. C. Boyd, R. C. Shallice, T. Moot, R. Kerner, L. Bertoluzzi, A. Onno, S. Kavadiya, C. Chosy, E. J. Wolf, J. Werner,



- J. A. Raiford, C. de Paula, A. F. Palmstrom, Z. J. Yu, J. J. Berry, S. F. Bent, Z. C. Holman, J. M. Luther, E. L. Ratcliff, N. R. Armstrong and M. D. McGehee, *Joule*, 2020, **4**, 1759–1775.
- 24 J. Zhang, J. Long, Z. Huang, J. Yang, X. Li, R. Dai, W. Sheng, L. Tan and Y. Chen, *Chem. Eng. J.*, 2021, **426**, 131357.
- 25 X. Zhao, J. Zhou, S. Wang, L. Tan, M. Li, H. Li and C. Yi, *ACS Appl. Energy Mater.*, 2021, **4**, 6903–6911.
- 26 L. Zheng, Y. Xuan, J. Wang, S. Bao, X. Liu and K. Zhang, *J. Mater. Chem. A*, 2022, **10**, 7251–7262.
- 27 N. Phung, M. Verheijen, A. Todinova, K. Datta, M. Verhage, A. Al-Ashouri, H. Kobler, X. Li, A. Abate, S. Albrecht and M. Creatore, *ACS Appl. Mater. Interfaces*, 2022, **14**, 2166–2176.
- 28 S. Zhumagali, F. H. Isikgor, P. Maity, J. Yin, E. Ugur, M. De Bastiani, A. S. Subbiah, A. J. Mirabelli, R. Azmi, G. T. Harrison, J. Troughton, E. Aydin, J. Liu, T. Allen, A. u. Rehman, D. Baran, O. F. Mohammed and S. De Wolf, *Adv. Energy Mater.*, 2021, **11**, 2101662.
- 29 M. Vosgueritchian, M. C. LeMieux, D. Dodge and Z. Bao, *ACS Nano*, 2010, **4**, 6137–6145.
- 30 Q. Wang, C.-C. Chueh, T. Zhao, J. Cheng, M. Eslamian, W. C. H. Choy and A. K.-Y. Jen, *ChemSusChem*, 2017, **10**, 3794–3803.
- 31 D. S. Mann, P. Patil, S.-N. Kwon and S.-I. Na, *Appl. Surf. Sci.*, 2021, **560**, 149973.
- 32 Y. Bai, H. Chen, S. Xiao, Q. Xue, T. Zhang, Z. Zhu, Q. Li, C. Hu, Y. Yang, Z. Hu, F. Huang, K. S. Wong, H.-L. Yip and S. Yang, *Adv. Funct. Mater.*, 2016, **26**, 2950–2958.
- 33 S. Hietzschold, S. Hillebrandt, F. Ullrich, J. Bombsch, V. Rohnacher, S. Ma, W. Liu, A. Köhn, W. Jaegermann, A. Pucci, W. Kowalsky, E. Mankel, S. Beck and R. Lovrincic, *ACS Appl. Mater. Interfaces*, 2017, **9**, 39821–39829.
- 34 J. Tirado, M. Vásquez-Montoya, C. Roldán-Carmona, M. Ralaarisoa, N. Koch, M. K. Nazeeruddin and F. Jaramillo, *ACS Appl. Energy Mater.*, 2019, **2**, 4890–4899.
- 35 Y. Zhang, S. Zhang, S. Wu, C. Chen, H. Zhu, Z. Xiong, W. Chen, R. Chen, S. Fang and W. Chen, *Adv. Mater. Interfaces*, 2018, **5**, 1800645.
- 36 F. Zhang, S. H. Silver, N. K. Noel, F. Ullrich, B. P. Rand and A. Kahn, *Adv. Energy Mater.*, 2020, **10**, 1903252.
- 37 L. Luo, Y. Zhang, N. Chai, X. Deng, J. Zhong, F. Huang, Y. Peng, Z. Ku and Y.-B. Cheng, *J. Mater. Chem. A*, 2018, **6**, 21143–21148.
- 38 M. T. Weller, O. J. Weber, J. M. Frost and A. Walsh, *J. Phys. Chem. Lett.*, 2015, **6**, 3209–3212.
- 39 R. H. Bube, *J. Appl. Phys.*, 1962, **33**, 1733–1737.
- 40 D. Shi, V. Adinolfi, R. Comin, M. Yuan, E. Alarousu, A. Buin, Y. Chen, S. Hoogland, A. Rothenberger, K. Katsiev, Y. Losovyj, X. Zhang, P. A. Dowben, O. F. Mohammed, E. H. Sargent and O. M. Bakr, *Science*, 2015, **347**, 519–522.

